Sharpness in motion corrected quantitative imaging at 7T

Bazin, Pierre Louis; Nijsse, Hannah E.; van der Zwaag, Wietske; Gallichan, Daniel; Alkemade, Anneke; Vos, Frans M.; Forstmann, Birte U.; Caan, Matthan W.A.

DOI
10.1016/j.neuroimage.2020.117227

Publication date
2020

Document Version
Final published version

Published in
NeuroImage

NeuroImage 222 (2020) 117227

Contents lists available at ScienceDirect

NeuroImage

journal homepage: www.elsevier.com/locate/neuroimage

Sharpness in motion corrected quantitative imaging at 7T

Pierre-Louis Bazin[a], Hannah E. Nijsse[b], Wietske van der Zwaag[c], Daniel Gallichan[d], Anneke Alkemade[a], Frans M. Vos[b], Birte U. Forstmann[a], Matthan W.A. Caan[e,*]

[a] Integrative Model-based Cognitive Neuroscience research unit, Department of Psychology, University of Amsterdam, Amsterdam, the Netherlands
[b] Department of Imaging Physics, Delft University of Technology, Delft, the Netherlands
[c] Spinoza Centre for Neuroimaging, Amsterdam, the Netherlands
[d] CUBRIC, School of Engineering, Cardiff University, Cardiff, United Kingdom
[e] Amsterdam UMC, University of Amsterdam, Biomedical Engineering and Physics, Amsterdam, the Netherlands

ARTICLE INFO

Keywords:
Motion correction
Sharpness quantification
Quantitative Imaging
Fat navigators
High-field MRI

ABSTRACT

Sub-millimeter imaging at 7T has opened new possibilities for qualitatively and quantitatively studying brain structure as it evolves throughout the life span. However, subject motion introduces image blurring on the order of magnitude of the spatial resolution and is thus detrimental to image quality. Such motion can be corrected for, but widespread application has not yet been achieved and quantitative evaluation is lacking. This raises a need to quantitatively measure image sharpness throughout the brain. We propose a method to quantify sharpness of brain structures at sub-voxel resolution, and use it to assess to what extent limited motion is related to image sharpness.

The method was evaluated in a cohort of 24 healthy volunteers with a wide and uniform age range, aiming to arrive at results that largely generalize to larger populations. Using 3D fat-excited motion navigators, quantitative R_1, R_2^* and Quantitative Susceptibility Maps and T_1-weighted images were retrospectively corrected for motion. Sharpness was quantified in all modalities for selected regions of interest (ROI) by fitting the sigmoidally shaped error function to data within locally homogeneous clusters. A strong, almost linear correlation between motion and sharpness improvement was observed, and motion correction significantly improved sharpness. Overall, the Full Width at Half Maximum reduced from 0.88 mm to 0.70 mm after motion correction, equivalent to a 2.0 times smaller voxel volume. Motion and sharpness were not found to correlate with the age of study participants. We conclude that in our data, motion correction using fat navigators is overall able to restore the measured sharpness to the imaging resolution, irrespective of the amount of motion observed during scanning.

1. Introduction

Throughout the life span, the brain develops and ages both on the macro- and microscopic level, with large variations in volume of brain structures, myelination and iron deposition (Acosta-Cabronero et al., 2016; Lebel et al., 2012; Yeatman et al., 2014). In vivo sub-millimeter imaging at ultra-high field strength (7T and higher) has opened up new possibilities for studying these processes quantitatively at an unprecedented level of detail (Caan et al., 2019; Keuken et al., 2017; Waehnert et al., 2016). With the increase in spatial resolution and consequently longer scanning times, subject motion is clearly an increasingly important topic of study. Examples of unavoidable motion are breathing, cardiac motion, sneezing and blinking. In other cases, such as anxiety, discomfort or hyperactivity, motion can be minimized by proper preparation and instruction (Godenschweger et al., 2016). Still, involuntary subject motion is on the order of magnitude of the imaging resolution and therefore degrading image quality (Herbst et al., 2014; Stucht et al., 2015). Ultra-high resolution imaging therefore often requires motion correction embedded in acquisition and reconstruction. Extreme examples include imaging at 350 μm resolution using retrospective FatNav motion correction (Federau and Gallichan, 2016), as well as 250 μm resolution T_1-weighted imaging and 150 μm resolution Time-of-Flight angiography using prospective marker-based motion correction (Lüsebrink et al., 2017; Mattern et al., 2018).

To allow for reliable application of motion correction techniques, their robustness in larger cohorts with a varying age range needs to

* Corresponding author.
E-mail addresses: pilou.bazin@uva.nl (P.-L. Bazin), hannah.nijsse@gmail.com (H.E. Nijsse), w.vanderzwaag@spinozacentre.nl (W. van der Zwaag), gallichand@cardiff.ac.uk (D. Gallichan), jmalkemade@gmail.com (A. Alkemade), f.m.vos@tudelft.nl (F.M. Vos), B.U.Forstmann@uva.nl (B.U. Forstmann), m.w.a.caan@amsterdamumc.nl (M.W.A. Caan).

https://doi.org/10.1016/j.neuroimage.2020.117227
Received 9 March 2020; Received in revised form 3 July 2020; Accepted 31 July 2020
Available online 8 August 2020

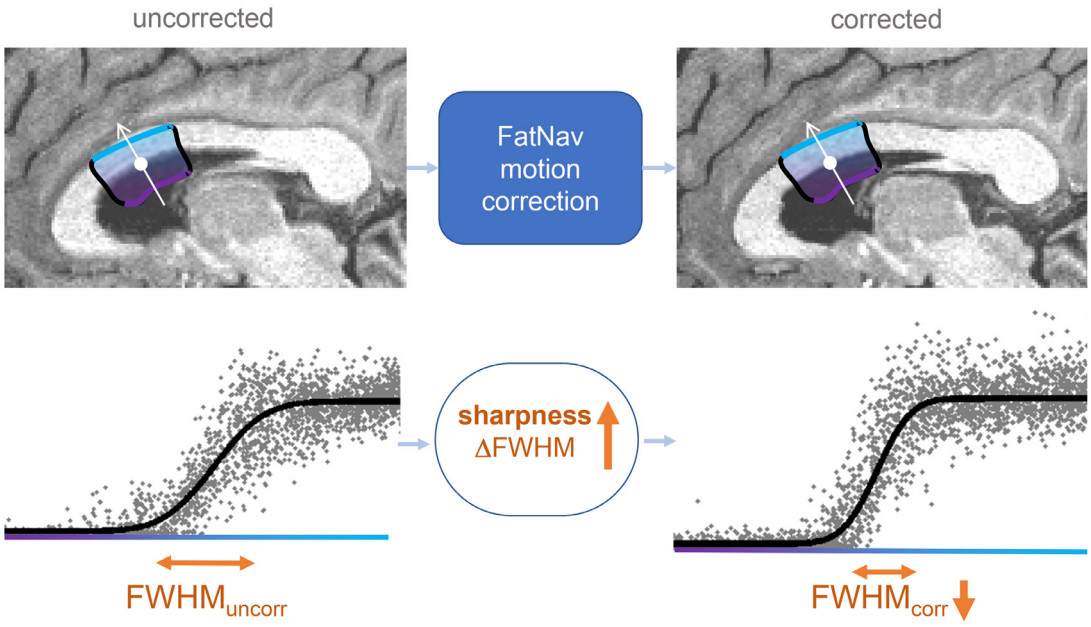

Fig. 1. Overview of our method. Using 3D fat-excited motion navigators, acquired data are retrospectively corrected for motion. Sharpness is quantified for selected regions of interest (ROIs, here illustrated for a ventricle) by fitting the sigmoidally shaped error function (erf) to data within locally homogeneous clusters over the edge of the ROI. A decrease in the full width at half maximum (ΔFWHM) of the error function after motion correction is indicative for increased sharpness in corrected data.

be demonstrated. In addition to visual inspection, quantitative information on the relation between the extent of motion and the improvement in image quality is needed. Such information can come from entropy minimization (Atkinson et al., 1999), the relative improvement in the metric used for motion correction (McGee et al., 2000) or signal in the air background (Mortamet et al., 2009). Other studies compared intensity differences before and after correction (Gallichan and Marques, 2017), computed the normalized gradient squared of the images (Gretsch et al., 2019; McGee et al., 2000), or studied segmentation repeatability (Kecskemeti and Alexander, 2020). These metrics enable to demonstrate an apparent improvement in image quality, but fail to quantify the actual improvement in apparent spatial resolution, perceived as the sharpness of the image.

Early work on super-resolution proposed fitting a sigmoid function to obtain the edge width as a measure of image resolution (Greenspan et al., 2002), an approach that was also followed in the field of electron microscopy (Rieger and van Veen, 2008). Here image sharpness was not defined as a physical measure related to distance but rather a rise in image intensity. Hence, it required constant-intensity objects to be applied on. Clearly, the human brain is a highly complex and anatomically variable organ, for which these conditions are not met. This raises a need for a method to measure image sharpness as in (Schoormans et al., 2020), applicable throughout the brain.

We propose a method to quantify sharpness over the edge width of specific brain structures, and use it to assess the improvement in resolution after motion correction. Our focus lies on assessing the effect of limited motion, i.e., around or below the imaging resolution, on image sharpness. We further aim to study to what extent motion is correlated with image sharpness. To this end, motion correction is performed retrospectively, such that differences between uncorrected and corrected data can be studied. Here we evaluate motion correction using 3D fat-excitation motion navigators (FatNavs) (Gallichan and Marques, 2017; Gretsch et al., 2019), an imaging based method exploiting the sparse fat signal circumscribing the brain as a proxy to determine rigid brain motion. The method is evaluated in a cohort of 24 healthy volunteers with a wide and uniform age range, aiming to arrive at results that mostly generalize to larger populations.

2. Theory

Obtaining a global measure for image sharpness in high resolution brain data is challenging for a number of reasons. First, since myelination and iron deposition patterns vary within anatomical structures (de Hollander et al., 2014; Marques and Norris, 2018; Tardif et al., 2015), quantitative parameters will not be constant. Second, variations in tissue signal can result in that only part of the tissue boundary will have sufficient contrast for image sharpness to be measurable. Third, limited Signal-to-Noise Ratio (SNR) challenges a robust estimate of sharpness in imaging data.

Fig. 1 provides an overview of our proposed method to address these challenges. Given a region of interest (ROIs), being a (sub)cortical brain structure, sharpness is defined along the transition boundary to the surrounding tissue. A sigmoidal function used to model the intensity transition and sharpness estimation over the ROI's edge is fitted to signal values, allowing for accurate estimation of the edge width and its uncertainty, given the amount of noise present in the data. The resulting sharpness estimate is defined in terms of physical distance, thus being invariant to scaling of input signal values. To account for local variability in tissue signal, a clustering approach is followed to define sharpness within sub-regions of similar tissue. Furthermore, calculations are restricted to clusters where sufficient contrast with the surrounding tissue is available, assessed by the model fit quality.

We now proceed by introducing our target function for sharpness estimation, followed by the clustering approach used to arrive at locally precise sharpness estimates, and our parameterization of motion.

2.1. Target function

While in the ideal situation the PSF of MRI can be considered to be an isotropic sinc(·) function (Wang et al., 2007), sequence limitations may introduce a directionality to the PSF. In the context of this work, the MP2RAGE-sequence, when acquired with Cartesian sequential partition-encoding, is presumed to have a directionality to its PSF due to T_1 relaxation (Marques et al., 2010). Subject motion during scanning is assumed to impose an additional detrimental effect on image resolution,

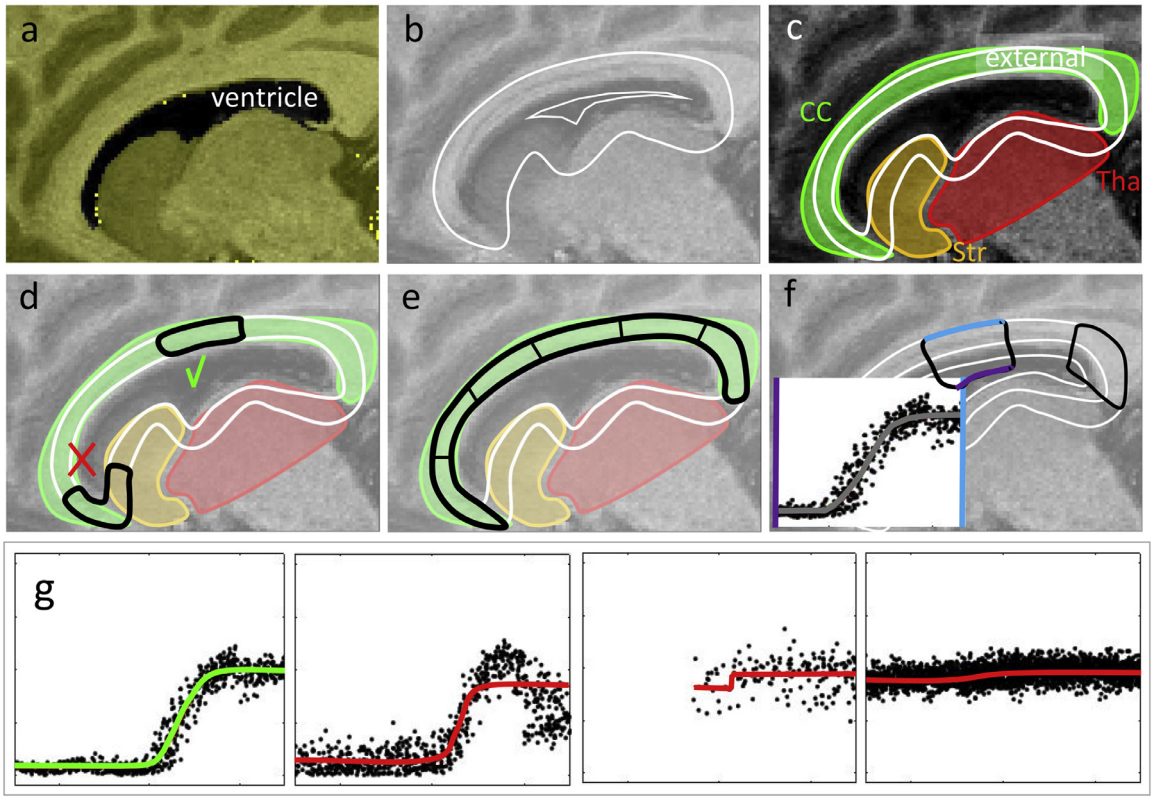

Fig. 2. Illustration of the clustering method. (a) Example ROI (ventricle) in black, (b) with a region enclosing the ROI-boundary used for sharpness measurement. (c) The external sub-region covers multiple anatomical structures (here: corpus callosum (CC), thalamus (Tha), striatum (Str)), (d) and clusters are to be found in homogeneous areas, in order to obtain unimodal intensity profiles as a function of signed distance to the ROI edge. (e) To this end, a two-step hierarchical k-means clustering is employed, to find spatially coherent clusters within homogeneous intensity areas. (f) Clusters are expanded back into the ROI for computing profiles, (g) and tested to be valid (green) or invalid (red) due to shape, insufficient data or high noise level or uncertainty.

with additional possibly anisotropic image blur and ghosting artifacts as a result (Hedley and Yan, 1992). Finally, given that sharpness is to be determined over tissue boundaries, a potential gradual change of tissue will further reduce the local apparent sharpness in the image.

Rather than explicitly modeling these additive effects on the PSF for our data, we are taking a utilitarian approach for the purpose of assessing the hypothesized improved sharpness after retrospective motion correction. First, the PSF is estimated locally, and here assumed to be Gaussian and isotropic, PSF $= \mathcal{G}(\sigma^2)$, with standard deviation σ. Second, motion is assumed to only increase σ and otherwise not affect the distribution. Third, a tissue boundary is assumed to be an edge function, which after undergoing the blurring effect of a Gaussian PSF yields a sigmoid function. Its profile can under these assumptions be described by a cumulative Gaussian function, also known as the error function (erf($\cdot$)). The measured signal as a function of distance $S(d)$ is then modeled as:

$$S(d) = S_0 + \frac{h}{2} \cdot \mathrm{erf}\left(\frac{d - d_c}{\sqrt{2}\sigma}\right) + \mathcal{N}(0, \tau^2). \quad (1)$$

Here S_0 is the signal offset, h is a scaling factor denoting the contrast difference over the edge width and d_c is a spatial offset to account for a possible local segmentation offset with respect to the current model. Additive normally distributed noise with variance τ^2 is assumed.

The standard deviation of uncorrected and corrected data $\sigma_{\mathrm{uncorr,corr}}$ is computed first. Sharpness is then inferred from the corresponding full width at half maximum, $\mathrm{FWHM}_{\mathrm{uncorr,corr}} = 2.36 \cdot \sigma_{\mathrm{uncorr,corr}}$, such that $\Delta\mathrm{FWHM} = \mathrm{FWHM}_{\mathrm{uncorr}} - \mathrm{FWHM}_{\mathrm{corr}}$ yields the improvement in sharpness.

2.2. Clustering

Selecting the data for error function fitting over the edge of a given ROI is commonly done along one dimension (1D). The procedure is then to select a point at the edge, determine the normal to the internal ROI surface in that point and sample data along a line. This approach has been implemented successfully for super-resolution in MRI (Greenspan et al., 2002) and in other fields of science, e.g., electron microscopy (Rieger and van Veen, 2008). A downside is that, given the low signal-to-noise ratio (SNR) in MRI, such an approach would sample insufficient data for reliable parameter fitting. Furthermore, the resolution of MRI is limited, even at ultra-high field strength, to both render a sufficiently densely sampled intensity profile and to precisely compute the normal to the ROI-surface that would be a prerequisite for unbiased sharpness estimation. Finally, the interpolation required to sample along arbitrary lines would reduce the sharpness we aim to measure.

We propose an alternative approach for estimating sharpness at sub-voxel resolution in noisy data. Fig. 2 illustrates the clustering procedure followed to arrive at spatially coherent regions for curve fitting. Through clustering, as specified below, locally homogeneous tissue is sampled on either side of the ROI-boundary, from 3 mm internal to 4 mm external. The external part is designed not to overlap with multiple anatomical structures (e.g. only the corpus callosum, see (Fig. 2c). The average cluster size is targeted to be 500 voxels (equivalent to a sphere with a radius of approximately 5 voxels). Thus, the total number of clusters per ROI can vary largely, dependent on its size. Within each cluster, each voxel is assigned its normal distance d to the boundary and the sigmoid function (Eq. (1)) is fitted to the normal distances, from which the FWHM for this cluster is obtained.

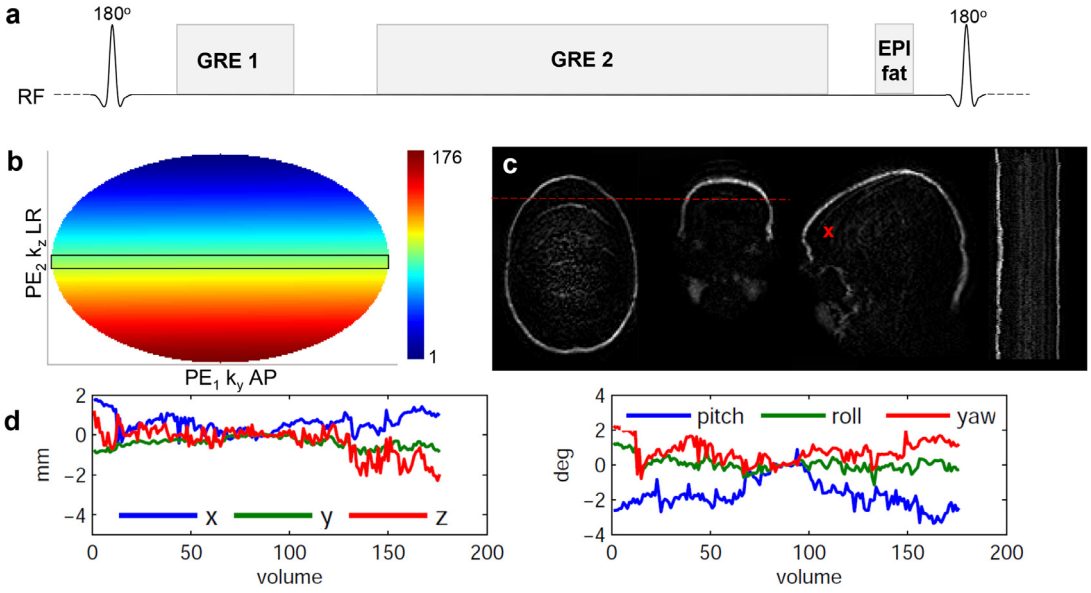

Fig. 3. (a) Sequence diagram with two gradient echo (GRE) readout blocks of variable lengths reading out one and four TEs respectively, and a 3D fat-exciting EPI navigator. (b) An elliptical shutter turbo readout is performed, colored per readout. The center (11 readouts, boxed) serves as anatomical reference during reconstruction. (c) Example 4D fat-navigator: transverse, coronal and sagittal slices at one time point, with to the right a space-time plot along the indicated red markers. (d) Corresponding translation and rotation parameters computed through rigid realignment.

In the abovementioned procedure, two stage k-means clustering is performed in the external region only (Fig. 2c). An initial clustering stage is run on z-transformed and concatenated spatial coordinates and signal values, so that contiguous regions with similar signal intensity are grouped together. Intensities are Gaussian smoothed with a standard deviation of 3 voxels to suppress noise (Fig. 2d). Four classes of tissue types are segmented in this initial clustering stage. A subsequent, more refined clustering is performed on spatial coordinates alone, separately within each of the initially obtained clusters (Fig. 2e). This stage aims to obtain spatially coherent clusters, something which is not guaranteed with signal value added as a feature during clustering. All voxels in the edge and internal part of the ROI are assigned to a cluster following a nearest neighbour rule to arrive at regions in which signal profiles are derived and curve fitting is performed (Fig. 2f).

2.3. Single motion parameter

To quantify general motion, we derive a single motion parameter m_{ROI} describing the extent of a rigid motion pattern over time within a given ROI. Previous work proposed k-space weighted motion metrics through partition-weighted integrated motion (Castella et al., 2018; Todd et al., 2015). Similar to (Dosenbach et al., 2017), we consider these to be estimated through rigid realignment on a series of N FatNavs images. For the realignment of image i to some reference image, we can define the rigid transformation matrix $T^{\mathbf{i}}$

$$T^i = \begin{bmatrix} \mathbf{R^i} & t^i \\ 0 & 1 \end{bmatrix}, \tag{2}$$

given an estimated rotation matrix $\mathbf{R^i}$ and translation vector $\mathbf{t^i} = t_x^i \quad t_y^i \quad t_z^{i\,T}$.

For each voxel in the brain, the displacement vector according to the FatNavs is calculated through $d^i(\vec{x}) = \left(T^{i^{-1}}\vec{x} - \vec{x}\right)$. For each ROI, the absolute mean ROI displacement is computed for each time point:

$$m^i_{\mathrm{ROI}} = \left| \int_{\vec{x}\in \mathrm{ROI}} d^i(\vec{x}) d\vec{x} \right| \tag{3}$$

The average extent of motion over time is defined as a weighted average over all estimated m^i_{ROI}

$$m_{\mathrm{ROI}} = \frac{1}{N}\sum_{i=1}^{N} w_i m^i_{\mathrm{ROI}}, \tag{4}$$

We opted for a Gaussian normalized weighting w_i with an empirically chosen FWHM of 50% of the second phase encoding dimension of k-space k_z. This normalization emphasized motion states which are centered in time, i.e., corresponding to the center of k-space in our sequence readout pattern (Fig. 3b), which dominates image contrast. Here, a motion-induced sampling error in only a few k-space points propagates to a large error in image domain. High-resolution spatial details are instead decomposed into a larger set of high frequencies scattered throughout k-space, much less likely to be affected by one instance of motion. Note that ideally this weighting of FatNavs were to be applied identically along both phase encoding dimensions. Practically, we were constrained by the scanners' line-by-line readout, such that each FatNav samples the entire first phase encoding dimension (apart from the elliptical shutter, Fig. 3b). Finally, a summarizing average motion parameter $m = \frac{1}{n}\sum_{ROIs} m_{\mathrm{ROI}}$ is estimated over n ROIs. For comparison purposes, the Framewise Displacement (FD) was computed, following the implementation in Dosenbach et al. (2017).

3. Experiments

3.1. Subjects

A subset of 24 participants from the AHEAD adult lifespan database (Alkemade et al., 2020) were selectively included to achieve sex balance (12 F) and a uniform age range distribution (between 21 and 81 years of age). The study was approved by the local ethical committee. All volunteers provided written informed consent to usage of their data for this study prior to participation.

3.2. Data acquisition

Volunteers were scanned at a 7 T scanner (Philips, Best, NL), equipped with a Nova Medical head coil (Wilmington MA, USA), con-

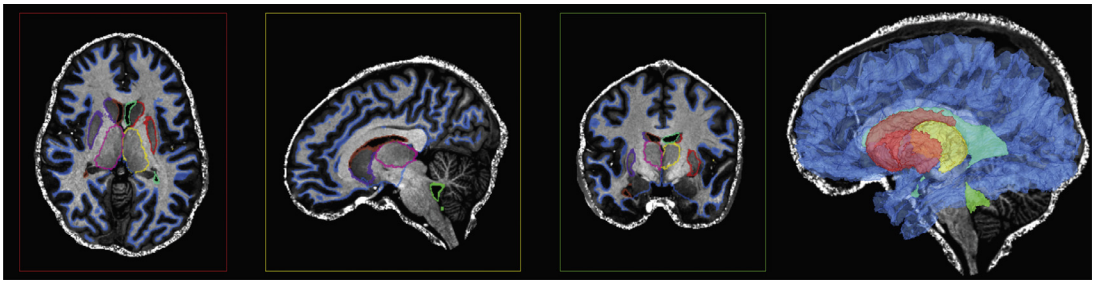

Fig. 4. Example outline of ROIs used in this study, with transverse, sagittal, and coronal slices, and plotted isosurfaces, including thalamus (pink/yellow), striatum (purple/red), ventricles (brown/green), 4th ventricle (light green) and cortical GM/WM boundary (blue).

taining a two-channel transmit and a 32-channel receive head coil. Second-order image based B_0-shimming was performed.

The sequence was built on top of the previously published MP2RAGEME (Magnetization Prepared 2 Rapid Acquisition Gradient Echoes Multi Echo) sequence (Caan et al., 2019) for simultaneous R_1, R_2^* and QSM mapping (see Fig. 3(a)). Briefly, in this sequence two different gradient echo (GRE) blocks are read out after an inversion pulse, the first being a single echo and second a multi echo readout. This flexible design allows for longer echo times (TEs) in the second readout block while maintaining a short repetition time of the sequence ($TR_{MP2RAGEME}$). A 3D Echo Planar Imaging (3D-EPI) fat-exciting motion-navigator (FatNav) was inserted into the sequence after the two GRE readout blocks (Gallichan and Marques, 2017; Gretsch et al., 2019). The Multiple Interleaved Scanning Sequences (MISS) environment, as provided by the vendor, was used to alternately acquire the two gradient echo blocks and the fat-navigated EPI-readout. The total scanning time amounted to 17 min.

The sequence parameters of the two GRE readout blocks were: Field of View (FOV) 205 mm × 205 mm × 164 mm, 234 sagittal slices, voxel size 0.7 mm isotropic, fold-over direction AP, 150 lines per block, bandwidth 405 Hz, parallel imaging undersampling (APxFH) 2x1, elliptical shutter with sequential line-by-line k-space readout (see Fig. 3(b)), $TR_{MP2RAGEME} = 6.8$ s, inversion times $TI_1 = 0.67$ s and $TI_2 = 3.7$ s, repetition times $TR_1 = 6.2$ ms and $TR_2 = 31$ ms, first echo time TE = 3.0 ms for both readouts, for the second readout four echoes were acquired with ΔTE = 8.5 ms, flip angle 4° for both readouts.

For the FatNav-readout (see Fig. 3(c)), fat was selectively excited using a three-subpulse binomial excitation pulse. The sequence parameters were: FOV= 240 mm × 240 mm × 160 mm, resolution 2 mm isotropic, SENSE (APxRL) 4 × 2, half scan (Partial Fourier) 0.75 × 0.75, EPI-factor 29, TR = 15 ms, TE = 5.8 ms, flip angle 1°, total read-out duration 477 ms. Note that the frame rate corresponds to $TR_{MP2RAGEME} = 6.8$ s.

An additional coil sensitivity reference scan was acquired to perform a GRAPPA (generalized autocalibrating partially acquisitions (Griswold et al., 2002)) reconstruction. This GRE matched the FOV of the MP2RAGEME sequence, had a flip angle of 6° and a resolution of 2.0 mm isotropic. The scanning time was 42 s.

3.3. Motion correction and reconstruction

Motion correction and reconstruction were performed offline in Retro-MoCo-Box[1] (Gallichan and Marques, 2017) a Matlab (The MathWorks, Inc., Natick, MA) toolbox for retrospective motion-correction of 3D MRI k-space data. GRAPPA calibration data were used to interpolate undersampled GRE-data, with a kernel size of 2x2. FatNavs were rigidly realigned, i.e., with six Degrees Of Freedom (DOF), using Statistical Parametric Mapping software (SPM8) (Ashburner and Friston, 2005) (see Fig. 3(d)). Subsequently, registration parameters were interpolated in time, accounting for the elliptical shutter readout of subsequent shots (see Fig. 3(b)). The motion parameters of the 11 center FatNavs correspond to the readout of the center of k-space (see Fig. 3(b)) and were averaged and used as anatomical reference point during reconstruction.

Motion correction was performed per coil element, after GRAPPA reconstruction. All reconstructed *k*-space lines were assigned to the closest corresponding FatNav, and subsequently corrected for the translation and rotation components by multiplying by a phase factor and corresponding rotation. Subsequently, data were simultaneously regridded and Fourier transformed through the non-uniform Fast Fourier Transform (nuFFT) (Fessler and Sutton, 2003). Coil images m_j were combined using complex conjugated normalized sensitivity weighting $\hat{S}_j^H$, to obtain complex-valued images $m = \sum_{j=1}^{C} \hat{S}_j^H m_j$.

Finally, quantitative R_1, R_2^* and Quantitative Susceptibility Maps (QSM) maps were computed as described elsewhere (Caan et al., 2019; Liu et al., 2015). Motion uncorrected images and parameter maps were generated by omitting correction steps in an otherwise unchanged reconstruction pipeline.

3.4. Segmentation and clustering

R_1-maps were segmented using the Nighres toolbox (Huntenburg et al., 2018), and a set of (sub)-cortical ROIs was selected: the left/right/fourth ventricle, left/right thalamus and striatum, and the cortical GM/WM boundary for analysis (Fig. 4). The per-voxel distance to the ROI-boundary could be specified with sub-voxel precision using the computed segmentation, which provided a level-set representation (Bazin et al., 2014).

Clustering was performed according to the procedure mentioned in Section 2.2 (see Supplementary Fig. S3). To obtain the required correspondence for computing differences in sharpness between motion uncorrected and corrected data ΔFWHM (Eq. (2.1)), only one of these had to be segmented and clustered for analysis. We opted to segment motion corrected and not uncorrected data, because of the anticipated higher image quality. Furthermore, the objective function enabled to model a spatial offset in the boundary location (Eq. (1)), which compensates for small segmentation deviations between corrected and uncorrected data. Through these steps, and curve fitting validity assessment as described below, the required correspondence in clustering for comparative analysis could be obtained.

3.5. Sharpness measurement

R_1, R_2^*, QSM and T_1-weighted images were analyzed after motion correction. Within all clusters of all ROIs, signal profiles as a function of signed distance over the ROI-boundary were computed. Non-linear least squares fitting of the objective function (Eq. (1)) was performed in MATLAB using Levenberg-Marquardt optimization with bisquare robust weighting (Levenberg, 1944; Marquardt, 1963). Estimated parameter values, uncertainties and normalised error values were obtained.

Curve fitting validity was assessed using three criteria, that had to be met in both uncorrected and corrected data fits for a cluster to be con-

[1] https://github.com/dgallichan/retroMoCoBox

sidered valid. First, the relative confidence bound, obtained from the Cramér-Rao Lower Bound (CRLB) of σ had to be smaller than 50%. Second, the number of internal data points inside the ROI had to be more than 10% of the total number of points. Third, the noise level needed to be smaller than 50% of the estimated height h of the objective function, in which the noise level was obtained from the normalised error of the fit. Sharpness metrics for (un)corrected data $\text{FWHM}_{\text{uncorr,corr}}$ and the improvement ΔFWHM were computed for all clusters, and median values over ROIs and subjects were obtained. Similarly, the extent of motion m_{ROI} was computed. A one-way Analysis of Variance (ANOVA) on the ΔFWHM score of all clusters and subjects was conducted to assess a significant improvement in sharpness per subject in a post-hoc analysis, using SPSS (IBM, Armonk, NY).

Because of non-normally distributed data, non-parametric Spearman's correlation analyses between sharpness and motion were performed, from which correlation coefficients ρ were obtained. This was done both on the subject and ROI level.

To investigate potential effects of subject age, motion and sharpness were plotted against age at time of scanning, and non-parametric Spearman's correlation analyses were performed.

The source code for the clustering and sharpness assessment is made available online[2].

3.6. Evaluation and comparison against other metrics

To validate the choice for segmenting motion corrected and not uncorrected data, R_1-maps were analysed using motion uncorrected data as the reference, while sharpness was only determined in the cortical GM/WM boundary.

The presented method contains a number of parameters for which heuristically chosen parameter values are proposed. To assess the robustness against variation in these parameters, a number of settings were varied and the effects evaluated. The extent of the sampling region was changed, from 4 to 3 mm externally while maintaining a 3 mm internal region. Meanwhile, the outer layer used for clustering was increased from 1 mm to 2 mm. Furthermore, the cluster size was changed from 500 to 250 and 1000 voxels. Lastly, the relative confidence bound was changed from 50% down to 25% and up to 100%.

In an early study, Normalized Gradient Squared (NGS) and Gradient Entropy were reported as sensitive image metrics for studying the effect of motion correction (McGee et al., 2000). In the context of limited motion in this study, we expected NGS to be a more sensitive metric than the histogram-based entropy metric and therefore included NGS in the analysis, computed on R_1-maps.

MRI Quality Control (MRIQC) is a software package including a large set of metrics (Esteban et al., 2017), which are computed in a standardized way. Because of ill-defined background values, we computed MRIQC-metrics on R_1-maps for within-brain metrics only, and used the magnitude image of the second inversion with the shortest echo time $\text{INV}_{2,\text{TE1}}$ for image background related metrics.

For all metrics, we computed difference scores of uncorrected and corrected data, and considered a positive difference an improvement in image quality. We then exploratively analysed the ensemble of metrics, by performing one-sided Student's t-tests to assess the improvement, and non-parametric Spearman correlation tests to evaluate the relation to the extent of motion m. Based on the test results, a subset of most descriptive metrics was selected for comparison against the proposed sharpness metric.

The Framewise Displacement (FD) was correlated with m and FWHM-metrics of R_1 using non-parametric Spearman correlation tests.

Contrast-to-Noise Ratios (CNR) were computed for one participant experiencing median motion in all clusters for R_1 and R_2^*. The estimated height h (Eq. (1)) was used as contrast measure, and the Mean Absolute Difference (MAD) of the fitting residuals as robust noise measure, such that CNR=h/MAD.

4. Results

An example reconstruction of R_1-maps of uncorrected and corrected data in a selected subject is given in Fig. 5. The thalamus is a structure located deep inside the brain and this location might not be much affected by rotations of the head. Nevertheless, there is clear blurring visible of the ventricular border at the level of the thalamus, which is significantly reduced in the rightmost panel with the corrected image (white arrowhead). Similar sharpening can be seen at the CSF-WM and GM/WM boundaries (white diamonds). In Fig. 6, the result of motion correction on sharpness in the prefrontal cortical areas is shown for selected subjects with a visually observed increasing level of motion artifacts before correction. In the case of limited motion (average motion $m = 0.21$ mm), better visibility of a perivascular space and longitudinal fissure could be seen (Fig. 6a, white arrowhead/diamond). In the case of more apparent motion blurring ($m = 0.52$ mm), distinct improvement in sharpness at the sulcal GM/CSF boundary can be seen (Fig. 6b, white arrowhead), In the two selected subjects with the largest extent of motion, remarkable differences are seen, with significant residual ghosting in one ($m = 0.55$ mm, Fig. 6c) and restoration of image quality in the other subject ($m = 1.54$ mm, Fig. 6d). Detailed inspection of motion plots of these two subjects (Fig. S2) revealed respectively continuous oscillatory patterns and a large shift midway through the experiment.

Fig. 7 illustrates motion correction in R_1-, R_2^*- and QSM-maps. The anterior limb of the internal capsule appeared sharper in the corrected R_1 map (white arrowhead). Of note, enlarged Virchow-Robin spaces can be observed as hypointensities in the basal ganglia. In uncorrected data, one of these in the caudate nucleus was visible in the R_2^*-map only after motion correction (white arrowhead).

Over all subjects, the median and 95-percentile values of the extent of motion were $m = 0.21$ mm and 0.55 mm respectively. The median sharpness in motion uncorrected data was $\text{FWHM}_{\text{uncorr}} = 0.88$ mm, reducing to $\text{FWHM}_{\text{corr}} = 0.70$ mm in corrected data. The median improvement in ΔFWHM was 26%. Converted to voxel volume, this implies an effective 2.0 times larger voxel volume if no motion correction were applied. The One-way ANOVA on ΔFWHM revealed that all but one subject showed a significant improvement in sharpness (ΔFWHM = 0.12 mm, 95% confidence interval −0.03 − 0.27 mm), corresponding to the subject depicted in Fig. 6c.

Fig. 8 shows the summary sharpness metrics as a function of the extent of motion m for the quantitative as well as the T1-weighted images. Sharpness on average improved for all subjects in all modalities. For both the R_1 and the T_1-weighted images, a significant correlation between motion and sharpness was found in the uncorrected data and in the improvement score but not in the corrected data. Furthermore, the R_2^*-sharpness values did not correlate with motion with or without motion correction. Finally, QSM-sharpness values correlated with motion in both uncorrected and motion corrected images.

Focusing on R_1, one subject has relatively non-sharp corrected $\text{FWHM}_{\text{corr}} = 1.1$ mm, with no significant improvement ΔFWHM = 0.12 mm, in concordance with the ANOVA (Fig. 6c). One other subject experienced a large extent of motion ($m > 1.5$ mm, corresponding to the subject shown in (Fig. 6d)) but also shows the largest improvement in ΔFWHM.

Studying the sharpness in more detail on the ROI-level, as shown in Fig. 9 it can be seen that on average, the improvement is largest in the cortical GM/WM-boundary, and smallest in the thalamus. It also appeared that in the thalamus the lowest relative number of valid clusters was found, 38% and 37% respectively in left and right hemispheres, Table 1.

In the analysis of existing metrics as depicted in Fig. 10, selected metrics were the Normalized Gradient Squared (NGS), the Coefficient of Joint Variation (CJV) with which high values are associated with the

[2] https://doi.org/10.21942/uva.12220658.v1

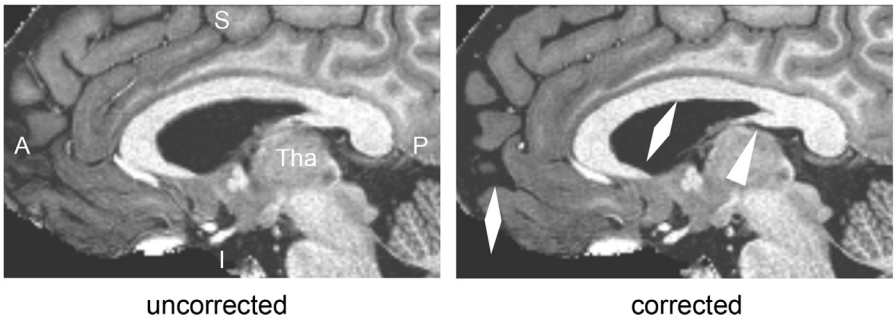

Fig. 5. Example cropped sagittal slice of an uncorrected and corrected R_1-map. The white arrowhead indicates the boundary of the thalamus (Tha). White diamonds point to CSF/GM and CSF/GM boundaries. See Fig. S1 for a plot for all included subjects.

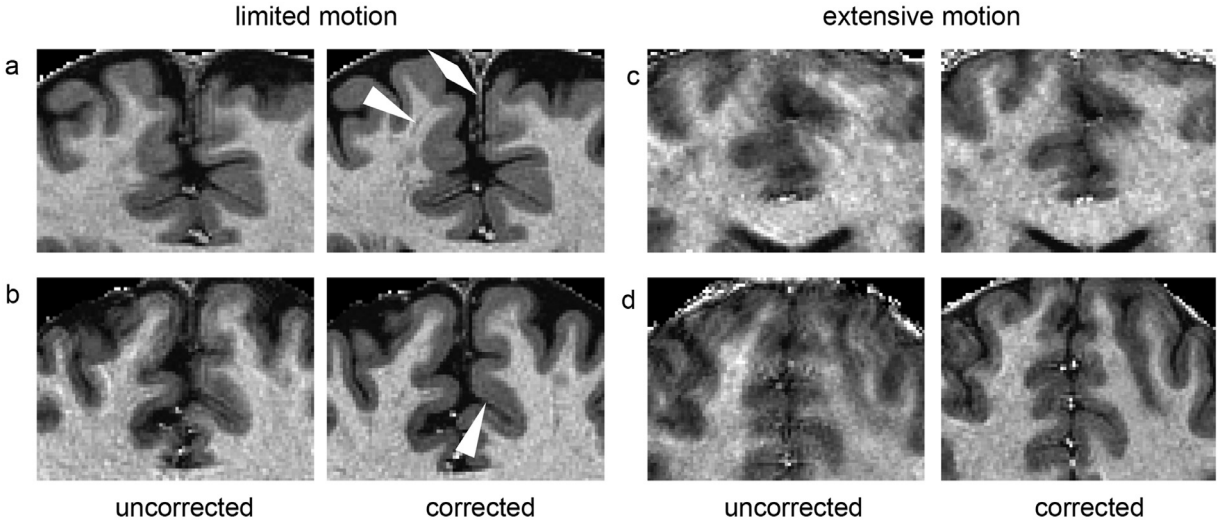

Fig. 6. Example cropped transverse slices of R_1-maps in the prefrontal cortex of selected subjects with increasing apparent level of motion artifacts before correction. (a) White arrowhead and diamond: perivascular space and longitudinal fissure. (b) White arrowhead: GM/CSF boundary. See Supplementary Fig. S2 for estimated motion parameters of these subjects.

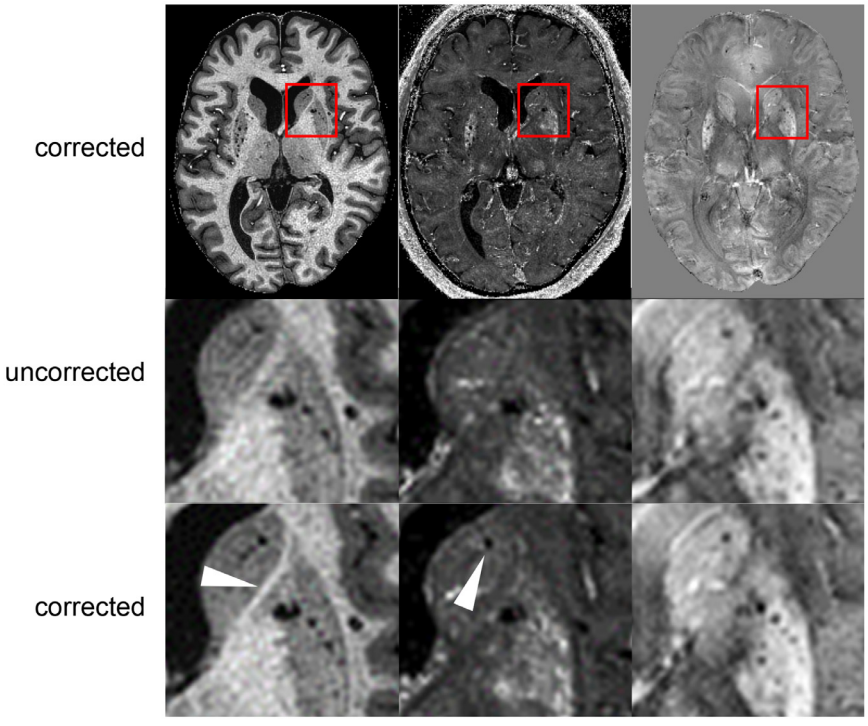

Fig. 7. Illustration of motion correction in multiple quantitative maps. From left to right: R_1, R_2^* and QSM. A transverse slice of motion corrected data (top) with an inset of uncorrected (center) and corrected data (bottom) is displayed. White arrowheads point to the anterior limb of the internal capsule (R_1) and an enlarged Virchow-Robin space (R_2^*) in corrected data insets.

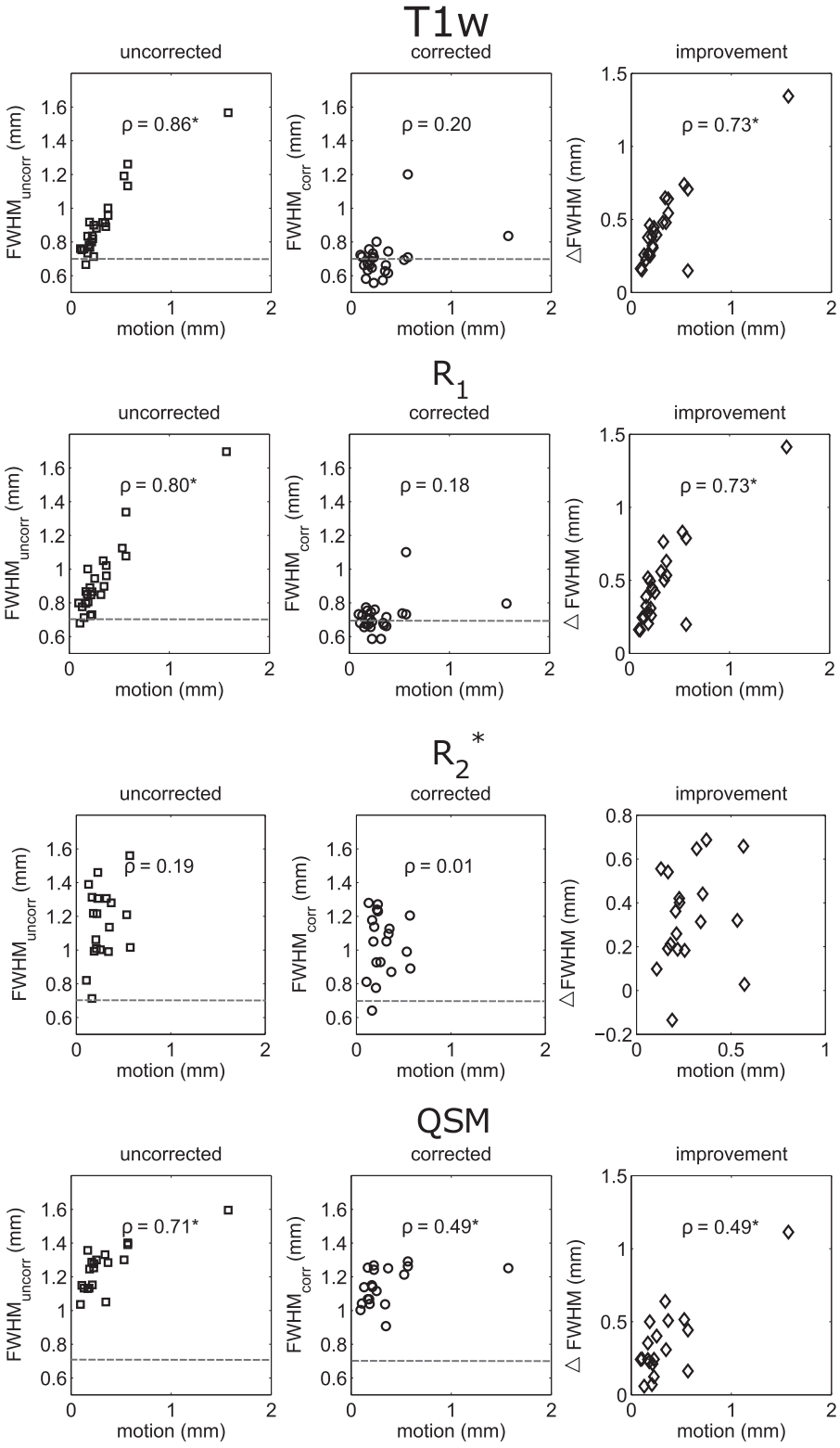

Fig. 8. Estimated median sharpness in R_1, R_2^*, QSM and T1-weighted images for all subjects in full width at half maximum (FWHM) in mm as a function of estimation motion in mm, in uncorrected and corrected data, with the improvement in sharpness. Spearman's correlation coefficient ρ is printed, where an asterisk (*) denotes significance ($p < 0.05$). The dashed line in the sharpness plot denotes the imaging resolution.

presence of motion artifacts (Poldrack et al., 2016), kurtosis in CSF k_{csf}, residual partial volume effect in CSF $rPVE_{csf}$, median background intensity bg_{med} and the amount of artifactual intensities in the air background QI_1 (Mortamet et al., 2009). This figure illustrates that this ensemble of metrics confirms a significant improvement in image quality, as well as a correlation of the improvement in image quality with motion. The metrics related to aliasing in the image background bg_{med} and QI_1 point to a measurable increase in apparent artifacts, correlated with the extent of motion in uncorrected and corrected data (bg_{med}).

The sharpness in FWHM and its uncertainty (Cramér-Rao Lower Bound, CRLB) were plotted against CNR for R_1 and R_2^* in two ROIs, the left and right ventricles, and the cortical GM/WM-boundary, see Fig. 11. CNR in R_1 is approximately twice as high as in R_2^*, and uncertainty correspondingly lower. Also for low CNR-values in the range

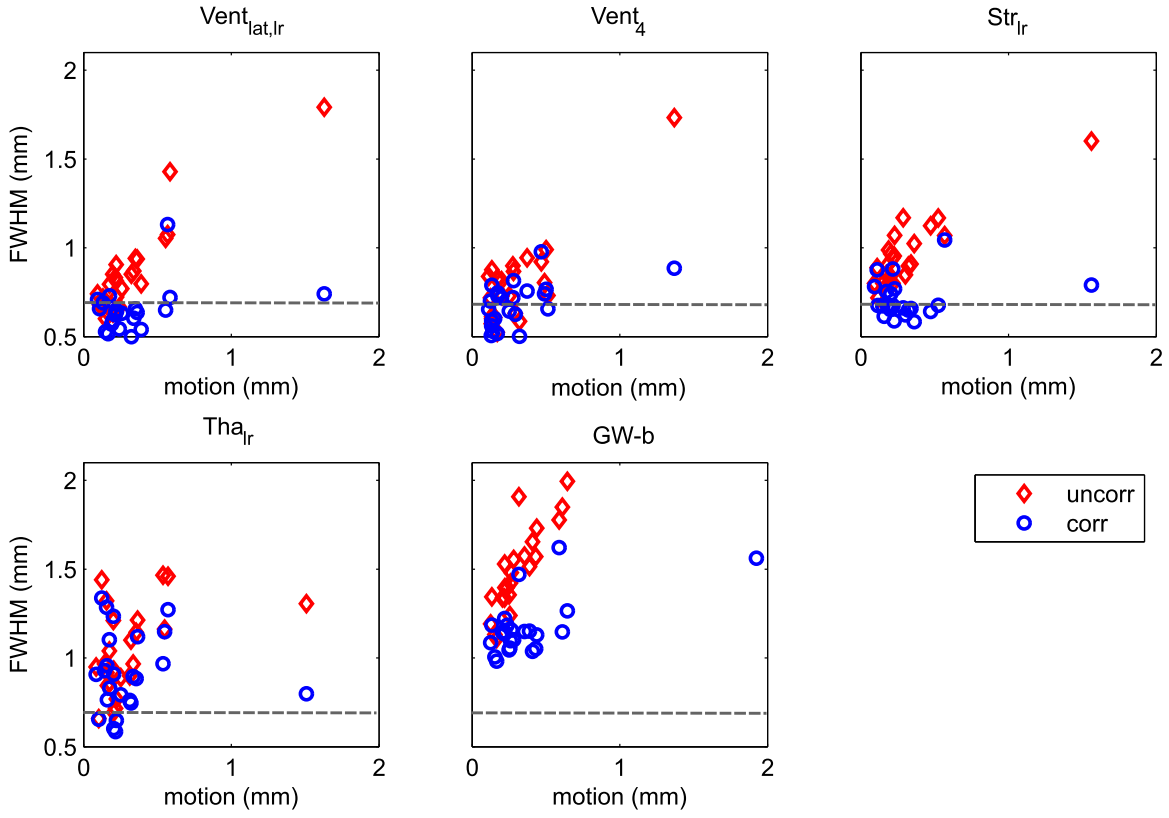

Fig. 9. Sharpness in uncorrected and corrected data $FWHM_{uncorr,corr}$, plotted per ROI, on median values over left and right hemispheres for ventricles, striatum, thalamus and the GM/WM-boundary. The dashed line denotes the acquired imaging resolution.

Table 1
Statistics on the Full Width at Half Maximum (FWHM) in uncorrected and corrected data (with Interquartile range) in mm, and relative number of valid clusters and total number of clusters (with standard deviations) per ROI: left/right lateral and fourth ventricle ($Ventr_{lat,lr,4}$), left/right striatum (Str_{lr}), left/right thalamus (Tha_{lr}), GM/WM-boundary (GW-b). FWHM-values are averaged over hemipheres.

ROI	$FWHM_{uncorr}$	$FWHM_{corr}$	clusters rel. valid	clusters total
$Ventr_{lat,lr}$	0.81 (0.22)	0.64 (0.09)	0.81 ± 0.10	28 ± 4
			0.77 ± 0.08	27 ± 3
$Ventr_4$	0.77 (0.26)	0.68 (0.18)	0.67 ± 0.09	8 ± 1
Str_{lr}	0.91 (0.22)	0.67 (0.11)	0.59 ± 0.12	25 ± 3
			0.58 ± 0.08	24 ± 2
Tha_{lr}	0.97 (0.34)	0.90 (0.35)	0.38 ± 0.11	16 ± 2
			0.37 ± 0.10	15 ± 1
GW-b	1.50 (0.35)	1.15 (0.11)	0.93 ± 0.06	533 ± 63

$2 < CNR < 5$, sufficient valid cluster fits are observed, albeit at higher uncertainty.

As a validation experiment, sharpness was computed at the cortical GM/WM boundary by segmenting motion uncorrected instead of corrected data. The obtained median (Interquartile Range) values were not dissimilar from those reported in Table 1, being $FWHM_{uncorr}$ = 1.51(0.34) mm and $FWHM_{corr}$ = 1.15(0.11) mm.

To assess the robustness of the method, heuristically chosen parameter values were varied. First, when changing the thickness of the external region from 1 to 2 mm and reducing the external sampling region from 4 to 3 mm while maintaining an internal region of 3 mm, the total number of clusters (computed in the external layer) approximately doubled, while cluster validity dropped by 20%. The reported FWHM in uncorrected and corrected data both increased by 4%. Subsequently, reducing the cluster size from 500 to 250 voxels led to an increase in FWHM of 7%, while an increase to 1000 voxels resulted in a large increase in FWHM by 27%. Lastly, the relative confidence bound was assessed. When increasing the bound for R_1 to 25% or 100%, the reported FWHM-values did not change. For 25%, all clusters in the thalamus were judged invalid, while changing to 100% resulted in a larger visually observed number of false positive cluster fits. For R_2^* (and QSM), we had to relax the validity constraint on uncertainty to 100%, to obtain a sufficient number of valid clusters (Figs. 8 and 11).

The proposed motion metric m was compared against the Framewise Displacement (FD). These metrics correlated significantly (ρ=0.49, p=0.015). The sharpness in uncorrected R_1-maps correlated significantly with FD (ρ=0.44), but the improvement in sharpness did not correlate with FD (ρ=0.17).

Fig. 12 shows no significant relation between age and correspondingly motion, uncorrected and corrected sharpness metrics ($p = 0.88$, $p = 0.88$, $p = 0.30$). The subject with unsuccessful motion correction was above 70 years of age, the subject with a large extent of motion and a large improvement younger than 25.

5. Discussion

We have presented a method for estimating sharpness in motion compensated quantitative imaging at 7T. Through a combined clustering and sigmoidally shaped error function curve fitting approach, sharpness could be locally estimated as the edge width of a selected set of segmented anatomical structures at sub-voxel resolution. The structures of choice characterized different regions and tissue contrasts in the brain, including cortical boundaries, deep subcortical structures, and the ventricular system. By performing retrospective motion correction using fat-excited motion navigators, we could precisely quantify the improvement in sharpness. We were able to show that this improvement corre-

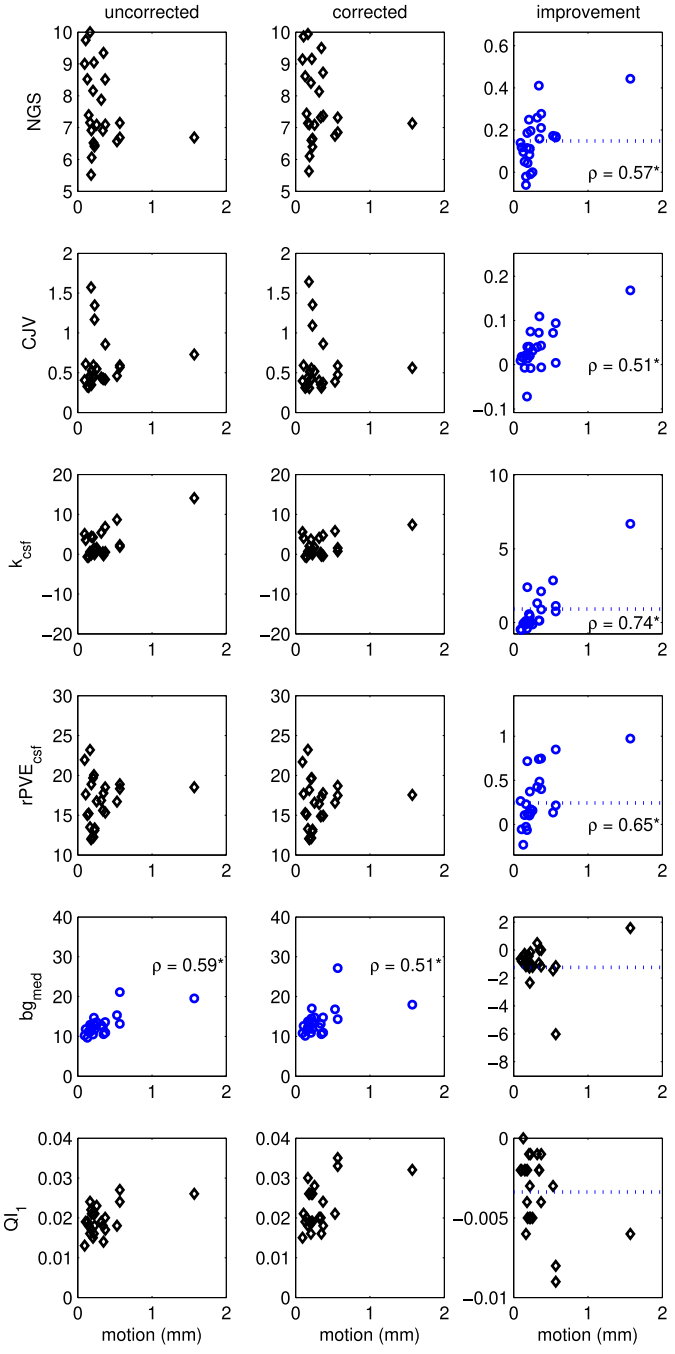

Fig. 10. Estimated median values for existing metrics in uncorrected and corrected R_1-maps data, with the improvement in sharpness, as a function of estimation motion in mm. Note the difference in scale for the improvement plots. Significant correlations are plotted in blue circles, with printed Spearman's correlation coefficients ρ. Dashed line denote a significant difference in improvement, with negative values implying a deterioration according to the metric. Refer to the text for an explanation of metrics.

lated significantly to the extent of motion experienced during scanning. Sharpness estimation was performed in a group of 24 subjects with a large and uniform age range covering the entire adult life span. Motion correction was illustrated to be feasible in multiparametric R_1-, R_2^*- and Quantitative Susceptibility Mapping (QSM)-data, as well as in T_1-weighted images.

In R_1-maps, motion correction significantly improved sharpness in all but one subject. Our sharpness metric did not point to a degraded image quality in any of the R_1-maps. In general, a strong, almost linear correlation between motion and sharpness improvement was observed. Computing motion per ROI averaged over clusters proved beneficial, since no correlation between the Framewise Displacement (FD) metric and the improvement in sharpness was observed. The median sharpness in motion uncorrected data was 0.88 mm, reducing to 0.70 mm in corrected data. The median improvement was 26%. Converted to voxel volume, this implies an effective 2.0 times larger voxel volume if no motion correction were applied.

With regard to R_2^*- and QSM-maps, an overall significant improvement in sharpness could also be demonstrated, using ROIs defined in R_1-maps. In uncorrected data, a significant correlation of sharpness with motion (with non-zero slope) is visible in QSM but not in R_2^* (Fig. 8). First, boundaries were defined on R_1, while R_2^* and QSM might not as systematically change on the same ROIs. Second, for R_2^*-maps, lower CNR and resulting higher uncertainty (CRLB) in the estimated FWHM as compared to R_1 (Fig. 11) are thought to be the underlying cause. Low CNR thus still allows for assessing the improvement in sharpness using our proposed metric, albeit with a reduced ability to measure edge information precisely enough to identify a relation between the improvement in sharpness and motion. Also, QSM, exploiting phase information, is more sensitive to motion effects as compared to R_2^*, estimated from magnitude data. However, QSM-maps after correction were still correlated with motion where R_1 was not, pointing to residual phase artifacts present in the data, possibly induced by B_0-fluctuations which were not corrected for.

Our results add to earlier work on motion correction in quantitative imaging in multi-parameter mapping (MPM) (Callaghan et al., 2015) and QSM (Mattern et al., 2019). With regard to the MPM-sequence, which comprises of a series of shorter acquisitions, we suspect that FatNav motion correction might lead to a smaller improvement but comparable final sharpness compared to the MP2RAGE-ME sequence. A limitation here would be that the acquisition time would have to be extended, because in contrast to the MP2RAGE-ME sequence no idle time is available to be exploited for the FatNav readouts in the GRE-readouts of MPM. In T_1-weighted images, nearly identical results as in R_1-maps were observed, illustrating that our method is generalizable to non-quantitative data. Future work should confirm our hypothesis that wide application in different weighted contrasts is feasible, also at 3T.

Sharpness in R_1 across all tested ROIs was improved by motion correction, from limited amounts (in the thalamus and fourth ventricle) to systematically large positive improvements (cortical WM boundary), see Table 1. We anticipate that subcortical structures, including the thalamus and fourth ventricle, experience less displacement than cortical structures such as the GM/WM cortical boundary. The relative number of valid clusters used in the estimation may further play a role here: only 38% of the clusters were valid for the thalamus, compared to well above 50% for the other structures. One explanation for this is the fact that the boundary of the thalamus with the neighboring WM of the internal capsule is very gradual, making the sigmoid fit not accurate enough over small windows. The fourth ventricle on the other hand has fairly reliable boundaries with the neighboring brainstem and cerebellum tissues, but is located in a region with increased pulsation artefact and lower overall SNR. And, due to its small size, only 8 clusters could be defined to estimate sharpness from. A strength of our study is the uniform and wide age distribution. We could see that everybody moves, regardless of age. This makes us confident to state that our metric can be successfully applied in a broader population.

The reported FWHM in corrected R_1- and T_1-weighted data falls below the imaging resolution of 0.7 mm for a subset of subjects. We attribute this to the Gaussian PSF that has been used. While this allows for a precise first order approximation to the sinc(·) function for measuring the improvement ΔFWHM, it may result in an systematically underestimated FWHM because of ignored Gibbs ringing.

The analysis of existing metrics showed that none of the tested metrics achieved the same strong correlations with motion as the proposed

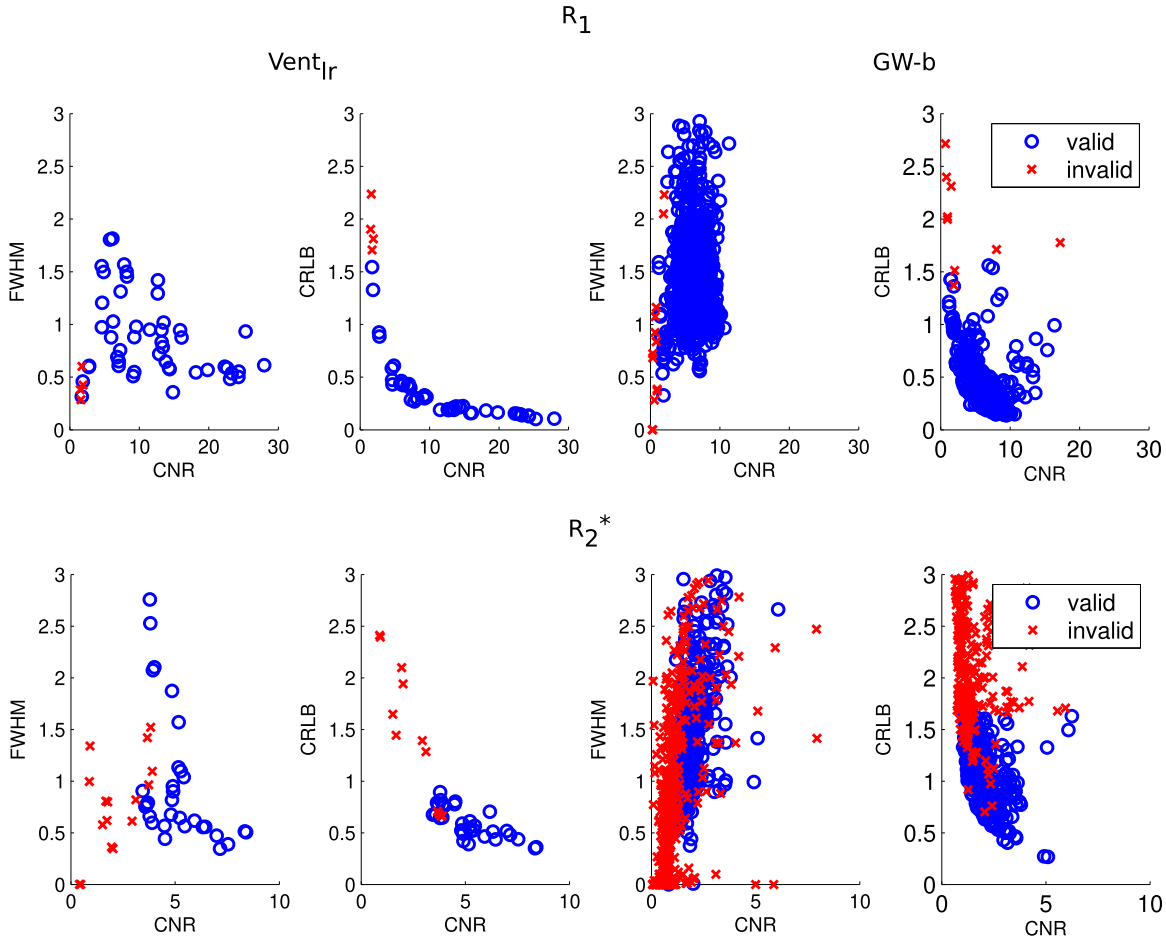

Fig. 11. Sharpness (FWHM) and its uncertainty (Cramér-Rao Lower Bound, CRLB) per cluster labeled by validity as a function of Contrast-to-Noise Ratio (CNR) for R_1 and R_2^* in two ROIs: left/right ventricles ($Vent_{lr}$) and GM/WM-boundary (GW-b). Note the different CNR-ranges for R_1 and R_2^*. Uncorrected and corrected data are jointly plotted.

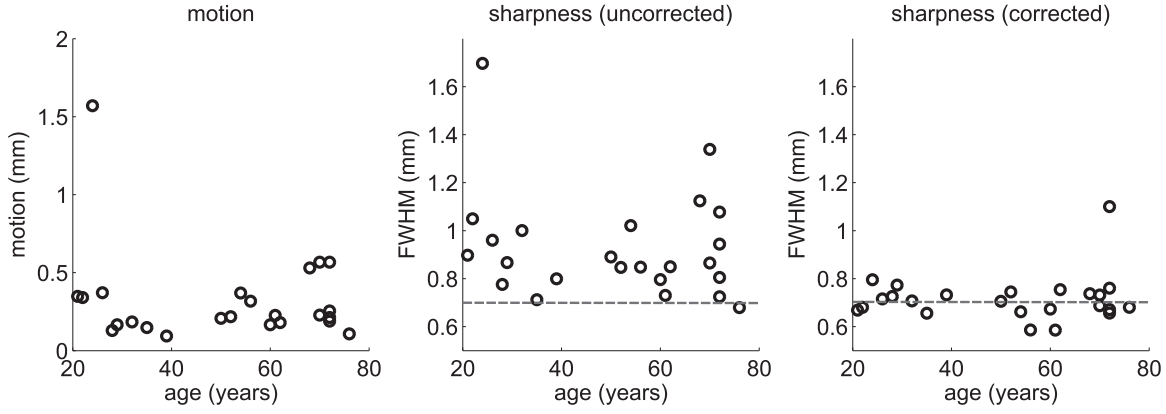

Fig. 12. Motion and sharpness in uncorrected and corrected data plotted as a function of age. The dashed line in the sharpness plot denotes the imaging resolution.

metric does. This could prove to be of added value, potentially also in the general MRI quality control setting (Esteban et al., 2017). Interestingly, the amount of aliasing in the background of the corrected data increased compared to the uncorrected data. Visual inspection indeed confirmed a minute increase in aliasing artifacts in the corrected image of a subject with extensive motion. We attribute this to the retrospective rotation of k-lines, such that the sampling pattern is no longer regular. This is a limitation of retrospective motion correction. Sparsity-constrained reconstruction using compressed sensing (Lustig et al., 2007) or deep learning (Lønning et al., 2019) were proposed as approaches to reconstruct irregularly sampled data.

We constrained ourselves to locally assessing image quality by quantifying sharpness at tissue boundaries, which imposes a limitation on the applicability of our approach. Motion-induced measurement errors in k-space propagate not only to a local blur but also to global aliasing artifacts throughout the Field-of-View, as was observed above. The latter effect is most prominent within the brain for large displacements. This was confirmed by the outcomes of our analysis, in the two sub-

jects showing the largest extent of motion. The first of the two showed significant aliasing artifacts that could not be corrected for, caused by higher frequency motion (Fig. 6(c), Supplementary Fig. S2). The second subject experienced a large shift midway through the scan, inducing a strong ghosting artifact jeopardizing our local sharpness quantification. The FatNavs could however accurately capture this motion pattern, resulting in a removal of the ghosting artifact and an improved and qualitatively restored image (Fig. 6(d)).

The second limitation of our approach is that the error function fitting needed to be computed over a certain spatial extent of 7 mm, for an imaging resolution of 0.7 mm. Small or thin anatomical structures are therefore challenging to assess, for instance at the GM/CSF boundary or within the brainstem. Furthermore, the requirement for intensity samples on both sides of the boundary makes it challenging to measure sharpness in highly curved regions. However, because we systematically discard regions with unreliable estimates, this measurement noise primarily biased the uncertainty of the sharpness estimation. Estimated FWHM-values proved to be invariant against changes in heuristically chosen parameter settings, provided that clusters remained sufficiently small (500 voxels) in order to locally sample tissue values. The validity criterion on uncertainty needed to be relaxed for the more noisy R_2^* and QSM data as compared to R_1 data, to balance between false positive and negative clusters. Indeed, CNR-values were on average a factor two lower in R_2^* than in R_1. Still, an average improvement in sharpness could be demonstrated.

Our work focused on retrospective motion correction using FatNavs only, which were initially proposed in 2D (Skare et al., 2015) and collapsed (Engström et al., 2015) form. In 3D, fat navigators were applied in ultra-high resolution imaging(Federau and Gallichan, 2016), and in a comparison against Moiré phase tracking, both methods were shown to result in excellent motion correction (Gretsch et al., 2019). Furthermore, application in the clinical setting of patients with brain tumors led to improvement in image quality (Glessgen et al., 2019). However, our method of sharpness quantification can be more broadly applied. In retrospective motion correction, other approaches to which our sharpness estimation could be applied include the use of 3D radial acquisitions (Anderson et al., 2013), field monitoring (Vannesjo et al., 2015) and FID navigators (Kober et al., 2011; Wallace et al., 2019). Prospective motion correction dates back more than 25 years ago (Maclaren et al., 2013), and the methods proposed include volumetric navigators (Kecskemeti and Alexander, 2020; Tisdall et al., 2012), fat navigators (Andersen, 2019; Boer, 2020; Truong, 2019), optical markers (Callaghan et al., 2015; Stucht et al., 2015; Todd et al., 2015), real-time field control (Özbay et al., 2017) and NMR field probes (Eschelbach et al., 2019). Prospective motion correction does not allow for a direct computation of the improvement in imaging sharpness. Reverse retrospective motion correction was proposed to demonstrate the improvement (Zahneisen et al., 2016). A cross-sectional comparison would be another approach to quantitatively evaluate sharpness for prospective motion correction using the proposed method. Alternatively, analyzing residual motion could be considered, such as in a cortical laminar fMRI-study at 9.4 Tesla (Bause et al., 2020).

Several studies indicate that motion differs with age, and between index and control groups (Greene et al., 2016). Additionally, differences in motion may, at least in part, explain differences observed in MRI measures. In the adult population above 20 years of age, a significant positive association between age and the extent of motion was found in a cohort of 266 subjects (Savalia et al., 2017). Note that our study was not powered to confirm this relation in our data (Fig. 12). Conversely, in the pediatric population below 20 years of age, a significant negative relation was found (Dosenbach et al., 2017). Importantly, head motion during scanning was shown to affect both structural (Brown et al., 2010) and functional pediatric imaging (Greene et al., 2018), and reduce gray matter volume and cortical thickness measures in adults (Reuter et al., 2015). Effects of motion were also demonstrated in neuropsychiatric patient groups. A clinical ultra-high field studies indicated that motion significantly affected R_2^*-values in Alzheimer's patients (Versluis et al., 2010). Motion correction is thus indispensable to alleviate these biases which hamper quantitative comparisons between groups and may become an essential practice in modern neuroimaging.

Beyond evaluating the effectiveness of motion correction techniques and quantifying the patterns of motion in pediatric and clinical populations, the sharpness of anatomical boundaries might be a feature of interest for developmental and plasticity studies. Although regions where the error function fitting is not robust should be considered with caution, sharpness differences at the boundary between WM and GM may reflect differences in cortical and sub-cortical myelination (Dinse et al., 2015; Keuken et al., 2017; Tardif et al., 2016) which may reveal subtle and important differences in the underlying micro-circuits (Turner, 2019).

6. Conclusion

The proposed metric revealed that limited sub-voxel motion almost linearly affects the apparent resolution in most investigated parameter maps and image contrasts, and further allows to quantify the improvement in sharpness irrespective of the extent of motion in high resolution quantitative and weighted imaging.

Declaration of Competing Interest

M.W.A. Caan is shareholder of Nico-lab Ltd.

CRediT authorship contribution statement

Pierre-Louis Bazin: Methodology, Software, Formal analysis, Writing - original draft, Visualization. **Hannah E. Nijsse:** Methodology, Software, Validation, Formal analysis, Writing - original draft. **Wietske van der Zwaag:** Methodology, Writing - review & editing. **Daniel Gallichan:** Methodology, Writing - review & editing. **Anneke Alkemade:** Funding acquisition, Writing - review & editing. **Frans M. Vos:** Methodology, Writing - review & editing. **Birte U. Forstmann:** Funding acquisition, Supervision, Writing - review & editing. **Matthan W.A. Caan:** Conceptualization, Methodology, Software, Validation, Formal analysis, Supervision, Writing - original draft.

Acknowledgements

The authors would like to thank dr. P.F. Buur and J. Castro for their support and M. Mulder, N, van Berendonk and N. Lutte for helping with the data collection. This work was partly supported by a NWO STW (AA, BUF), and a NWO Vici (BUF) grant. This publication is based on the STAIRS project under the TKI-PPP program. The collaboration project is co-funded by the PPP Allowance made available by Health Holland, Top Sector Life Sciences & Health, to stimulate public-private partnerships.

Supplementary material

Supplementary material associated with this article can be found, in the online version, at 10.1016/j.neuroimage.2020.117227.

References

Acosta-Cabronero, J., Betts, M.J., Cardenas-Blanco, A., Yang, S., Nestor, P.J., 2016. In vivo MRI mapping of brain iron deposition across the adult lifespan. J. Neurosci. 36 (2), 364–374. doi:10.1523/JNEUROSCI.1907-15.2016.

Alkemade, A., Mulder, M.J., Groot, J.M., Isaacs, B.R., van Berendonk, N., Lute, N., Isherwood, S.J., Bazin, P.-L., Forstmann, B.U., 2020. The Amsterdam Ultra-high field adult lifespan database (AHEAD): A freely available multimodal 7 Tesla submillimeter magnetic resonance imaging database. NeuroImage 117200. doi:10.1016/j.neuroimage.2020.117200.

Andersen, M., 2019. PLoS ONE. doi:10.1371/journal.pone.0217145.

Anderson, A.G., Velikina, J., Block, W., Wieben, O., Samsonov, A., 2013. Adaptive retrospective correction of motion artifacts in cranial MRI with multicoil three-dimensional radial acquisitions. Magn. Reson. Med. 69 (4), 1094–1103. doi:10.1002/mrm.24348.

Ashburner, J., Friston, K.J., 2005. Unified segmentation. NeuroImage 26 (3), 839–851. doi:10.1016/j.neuroimage.2005.02.018.

Atkinson, D., Hill, D.L., Stoyle, P.N., Summers, P.E., Clare, S., Bowtell, R., Keevil, S.F., 1999. Automatic compensation of motion artifacts in MRI. Magnetic Resonance in Medicine 41 (1), 163–170. doi:10.1002/(SICI)1522-2594(199901)41:1<163::AID-MRM23>3.0.CO;2-9

Bause, J., Polimeni, J.R., Stelzer, J., In, M.H., Ehses, P., Kraemer-Fernandez, P., Aghaeifar, A., Lacosse, E., Pohmann, R., Scheffler, K., 2020. Impact of prospective motion correction, distortion correction methods and large vein bias on the spatial accuracy of cortical laminar fMRI at 9.4 Tesla. NeuroImage 208, 116434. doi:10.1016/j.neuroimage.2019.116434.

Bazin, P.L., Weiss, M., Dinse, J., Schäfer, A., Trampel, R., Turner, R., 2014. A computational framework for ultra-high resolution cortical segmentation at 7 Tesla. NeuroImage 93, 201–209. doi:10.1016/j.neuroimage.2013.03.077.

Boer, V., 2020. Magnetic Resonance in Medicine. doi:10.1002/mrm.28202.

Brown, T.T., Kuperman, J.M., Erhart, M., White, N.S., Roddey, J.C., Shankaranarayanan, A., Han, E.T., Rettmann, D., Dale, A.M., 2010. Prospective motion correction of high-resolution magnetic resonance imaging data in children. NeuroImage 53 (1), 139–145. doi:10.1016/j.neuroimage.2010.06.017.

Caan, M.W., Bazin, P.L., Marques, J.P., de Hollander, G., Dumoulin, S.O., van der Zwaag, W., 2019. MP2RAGEME: T1, T2*, and QSM mapping in one sequence at 7 tesla. Hum. Brain Map. 40 (6), 1786–1798. doi:10.1002/hbm.24490.

Callaghan, M.F., Josephs, O., Herbst, M., Zaitsev, M., Todd, N., Weiskopf, N., 2015. An evaluation of prospective motion correction (PMC) for high resolution quantitative MRI. Front. Neurosci. 9 (MAR), 1–9. doi:10.3389/fnins.2015.00097.

Castella, R., Arn, L., Dupuis, E., Callaghan, M.F., Draganski, B., Lutti, A., 2018. Controlling motion artefact levels in MR images by suspending data acquisition during periods of head motion. Magn. Reson. Med. 80 (6), 2415–2426. doi:10.1002/mrm.27214.

Dinse, J., Härtwich, N., Waehnert, M., Tardif, C., Schäfer, A., Geyer, S., Preim, B., Turner, R., Bazin, P.-L., 2015. A cytoarchitecture-driven myelin model reveals area-specific signatures in human primary and secondary areas using ultra-high resolution in-vivo brain MRI. NeuroImage 114, 71–87. doi:10.1016/j.neuroimage.2015.04.023.

Dosenbach, N.U., Koller, J.M., Earl, E.A., Miranda-Dominguez, O., Klein, R.L., Van, A.N., Snyder, A.Z., Nagel, B.J., Nigg, J.T., Nguyen, A.L., Wesevich, V., Greene, D.J., Fair, D.A., 2017. Real-time motion analytics during brain MRI improve data quality and reduce costs. NeuroImage 161 (January), 80–93. doi:10.1016/j.neuroimage.2017.08.025.

Engström, M., Mårtensson, M., Avventi, E., Norbeck, O., Skare, S., 2015. Collapsed Fat Navigators for Brain 3D Rigid Body Motion. Magnetic Resonance Imaging 33 (8), 984–991. doi:10.1016/j.mri.2015.06.014.

Eschelbach, M., Aghaeifar, A., Bause, J., Handwerker, J., Anders, J., Engel, E.M., Thielscher, A., Scheffler, K., 2019. Comparison of prospective head motion correction with NMR field probes and an optical tracking system. Magn. Reson. Med. 81 (1), 719–729. doi:10.1002/mrm.27343.

Esteban, O., Birman, D., Schaer, M., Koyejo, O.O., Poldrack, R.A., Gorgolewski, K.J., 2017. MRIQC: advancing the automatic prediction of image quality in MRI from unseen sites. PLoS One 12 (9), e0184661. doi:10.1371/journal.pone.0184661.

Federau, C., Gallichan, D., 2016. Motion-correction enabled ultra-high resolution in-vivo 7T-MRI of the brain. PLoS One 11 (5), e0154974. doi:10.1371/journal.pone.0154974.

Fessler, J.A., Sutton, B.P., 2003. Nonuniform fast Fourier transforms using min-max interpolation. IEEE Trans. Signal Process. 51 (2), 560–574. doi:10.1109/TSP.2002.807005.

Gallichan, D., Marques, J.P., 2017. Optimizing the acceleration and resolution of three-dimensional fat image navigators for high-resolution motion correction at 7T. Magn. Reson. Med. 77 (2), 547–558. doi:10.1002/mrm.26127.

Glessgen, C., Gallichan, D., Moor, M., Hainc, N., Federau, C., 2019. Evaluation of 3D fat-navigator based retrospective motion correction in the clinical setting of patients with brain tumors. Neuroradiology 61 (5), 557–563. doi:10.1007/s00234-019-02160-w.

Godenschweger, F., Kägebein, U., Stucht, D., Yarach, U., Sciarra, A., Yakupov, R., Lüsebrink, F., Schulze, P., Speck, O., 2016. Motion correction in MRI of the brain. 10.1088/0031-9155/61/5/R32

Greene, D.J., Black, K.J., Schlaggar, B.L., 2016. Considerations for MRI study design and implementation in pediatric and clinical populations. Devel. Cognit. Neurosci. 18, 101–112. doi:10.1016/j.dcn.2015.12.005.

Greene, D.J., Koller, J.M., Hampton, J.M., Wesevich, V., Van, A.N., Nguyen, A.L., Hoyt, C.R., McIntyre, L., Earl, E.A., Klein, R.L., Shimony, J.S., Petersen, S.E., Schlaggar, B.L., Fair, D.A., Dosenbach, N.U., 2018. Behavioral interventions for reducing head motion during MRI scans in children. NeuroImage 171 (January), 234–245. doi:10.1016/j.neuroimage.2018.01.023.

Greenspan, H., Oz, G., Kiryati, N., Peled, S.L.B.G., 2002. MRI inter-slice reconstruction using super-resolution. Magn. Reson. Imaging 20, 437–446.

Gretsch, F., Mattern, H., Gallichan, D., Speck, O., 2019. Fat navigators and Moiré phase tracking comparison for motion estimation and retrospective correction. Magn. Reson. Med. (June 2019) 83–93. doi:10.1002/mrm.27908.

Griswold, M.A., Jakob, P.M., Heidemann, R.M., Nittka, M., Jellus, V., Wang, J., Kiefer, B., Haase, A., 2002. Generalized autocalibrating partially parallel acquisitions (GRAPPA).. Mag. Reson. Med. 47 (6), 1202–1210. doi:10.1002/mrm.10171.

Hedley, M., Yan, H., 1992. Motion artifact suppression: a review of post-processing techniques. Magn. Reson. Imaging 10 (4), 627–635. doi:10.1016/0730-725X(92)90014-Q.

Herbst, M., MacLaren, J., Lovell-Smith, C., Sostheim, R., Egger, K., Harloff, A., Korvink, J., Hennig, J., Zaitsev, M., 2014. Reproduction of motion artifacts for performance analysis of prospective motion correction in MRI. Magn. Reson. Med. 71 (1), 182–190. doi:10.1002/mrm.24645.

de Hollander, G., Keuken, M.C., Bazin, P.-L., Weiss, M., Neumann, J., Reimann, K., Wähnert, M., Turner, R., Forstmann, B.U., Schäfer, A., 2014. A gradual increase of iron toward the medial-inferior tip of the subthalamic nucleus.. Hum. Brain Map. 35 (9), 4440–4449. doi:10.1002/hbm.22485.

Huntenburg, J.M., Steele, C.J., Bazin, P.L., 2018. Nighres: processing tools for high-resolution neuroimaging. GigaScience 7 (7). doi:10.1093/gigascience/giy082.

Kecskemeti, S.R., Alexander, A.L., 2020. Test-retest of automated segmentation with different motion correction strategies: a comparison of prospective versus retrospective methods. NeuroImage 209, 116494. doi:10.1016/j.neuroimage.2019.116494.

Keuken, M.C., Bazin, P.-L., Backhouse, K., Beekhuizen, S., Himmer, L., Kandola, A., Lafeber, J.J., Prochazkova, L., Trutti, A., Schäfer, A., Turner, R., Forstmann, B.U., 2017. Effects of aging on $$T_{1}$$ T 1, $$T_{2}^{*}$$ T 2, and QSM MRI values in the subcortex. Brain Struct. Funct. 222 (6), 2487–2505. doi:10.1007/s00429-016-1352-4.

Kober, T., Marques, J.P., Gruetter, R., Krueger, G., 2011. Head motion detection using FID navigators. Magn. Reson. Med. 66 (1), 135–143. doi:10.1002/mrm.22797.

Lebel, C., Gee, M., Camicioli, R., Wieler, M., Martin, W., Beaulieu, C., 2012. Diffusion tensor imaging of white matter tract evolution over the lifespan.. NeuroImage 60 (1), 340–352. doi:10.1016/j.neuroimage.2011.11.094.

Levenberg, K., 1944. A method for the solution of certain non-linear problems in least squares. Q. Appl. Math. 2 (2), 164–168. doi:10.1090/qam/10666.

Liu, C., Li, W., Tong, K.a., Yeom, K.W., Kuzminski, S., 2015. Susceptibility-weighted imaging and quantitative susceptibility mapping in the brain. J. Magn. Reson. Imaging 42 (1), 23–41. doi:10.1002/jmri.24768.

Lønning, K., Putzky, P., Sonke, J.-J., Reneman, L., Caan, M.W., Welling, M., 2019. Recurrent inference machines for reconstructing heterogeneous MRI data. Med. Image Anal. 53, 64–78. doi:10.1016/j.media.2019.01.005.

Lüsebrink, F., Sciarra, A., Mattern, H., Yakupov, R., Speck, O., 2017. T1-weighted in vivo human whole brain MRI dataset with an ultrahigh isotropic resolution of 250 μm. Sci. Data 4, 170032. doi:10.1038/sdata.2017.32.

Lustig, M., Donoho, D., Pauly, J.M., 2007. Sparse MRI: the application of compressed sensing for rapid MR imaging.. Magn. Reson. Med. 58 (6), 1182–1195. doi:10.1002/mrm.21391.

Maclaren, J., Herbst, M., Speck, O., Zaitsev, M., 2013. Prospective motion correction in brain imaging: areview. Magn. Reson. Med. 69 (3), 621–636. doi:10.1002/mrm.24314.

Marquardt, D.W., 1963. An algorithm for least-squares estimation of nonlinear parameters. J. Soc. Ind. Appl.Math. 11 (2), 431–441. doi:10.1137/0111030.

Marques, J.P., Kober, T., Krueger, G., van der Zwaag, W., Van de Moortele, P.F., Gruetter, R., 2010. MP2RAGE, a self bias-field corrected sequence for improved segmentation and T1-mapping at high field. NeuroImage 49 (2), 1271–1281. doi:10.1016/j.neuroimage.2009.10.002.

Marques, J.P., Norris, D.G., 2018. How to choose the right MR sequence for your research question at 7 T and above? NeuroImage (April) 119–140. doi:10.1016/j.neuroimage.2017.04.044.

Mattern, H., Sciarra, A., Godenschweger, F., Stucht, D., Lüsebrink, F., Rose, G., Speck, O., 2018. Prospective motion correction enables highest resolution time-of-flight angiography at 7T. Magn. Reson. Med. 80 (1), 248–258. doi:10.1002/mrm.27033.

Mattern, H., Sciarra, A., Lüsebrink, F., Acosta-Cabronero, J., Speck, O., 2019. Prospective motion correction improves high-resolution quantitative susceptibility mapping at 7T. Magn. Reson. Med. 81 (3), 1605–1619. doi:10.1002/mrm.27509.

McGee, K.P., Manduca, A., Felmlee, J.P., Riederer, S.J., Ehman, R.L., 2000. Image metric-based correction (Autocorrection) of motion effects: Analysis of image metrics. J. Magn. Reson. Imaging 11 (2), 174–181. doi:10.1002/(SICI)1522-2586(200002)11:2<174::AID-JMRI15>3.0.CO;2-3.

Mortamet, B., Bernstein, M.A., Jack, C.R., Gunter, J.L., Ward, C., Britson, P.J., Meuli, R., Thiran, J.P., Krueger, G., 2009. Automatic quality assessment in structural brain magnetic resonance imaging. Magn. Reson. Med. 62 (2), 365–372. doi:10.1002/mrm.21992.

Özbay, P.S., Duerst, Y., Wilm, B.J., Pruessmann, K.P., Nanz, D., 2017. Enhanced quantitative susceptibility mapping (QSM) using real-time field control. Magn. Reson. Med. 778, 770–778. doi:10.1002/mrm.26735.

Poldrack, R., Congdon, E., Triplett, W., Gorgolewski, K., Karlsgodt, K., Mumford, J., Sabb, F., Freimer, N., London, E., Cannon, T., Bilder, R., 2016. A phenome-wide examination of neural and cognitive function. Sci. Data 3 (1), 160110. doi:10.1038/sdata.2016.110.

Reuter, M., Tisdall, M.D., Qureshi, A., Buckner, R.L., van der Kouwe, A.J., Fischl, B., 2015. Head motion during MRI acquisition reduces gray matter volume and thickness estimates. NeuroImage 107, 107–115. doi:10.1016/j.neuroimage.2014.12.006.

Rieger, B., van Veen, G. N. A., 2008. Method to determine image sharpness and resolution in Scanning Electron Microscopy images, 613–614. 10.1007/978-3-540-85156-1_307

Savalia, N.K., Agres, P.F., Chan, M.Y., Feczko, E.J., Kennedy, K.M., Wig, G.S., 2017. Motion-related artifacts in structural brain images revealed with independent estimates of in-scanner head motion. Hum. Brain Map. 38 (1), 472–492. doi:10.1002/hbm.23397.

Schoormans, J., Strijkers, G.J., Hansen, A.C., Nederveen, A.J., Coolen, B.F., 2020. Compressed sensing MRI with variable density averaging (CS-VDA) outperforms full sampling at low SNR.. Phys. Med. Biol. 65 (4), 045004. doi:10.1088/1361-6560/ab63b7.

Skare, S., Hartwig, A., Mårtensson, M., Avventi, E., Engström, M., 2015. Properties of a 2D fat navigator for prospective image domain correction of nodding motion in brain MRI. Magn. Reson. Med. 73 (3), 1110–1119. doi:10.1002/mrm.25234.

Stucht, D., Danishad, K.A., Schulze, P., Godenschweger, F., Zaitsev, M., Speck, O., 2015. Highest Resolution In Vivo Human Brain MRI Using Prospective Motion Correction. PLoS One 10 (7), e0133921. doi:10.1371/journal.pone.0133921.

Tardif, C.L., Gauthier, C.J., Steele, C.J., Bazin, P.-L., Schäfer, A., Schaefer, A., Turner, R., Villringer, A., 2016. Advanced MRI techniques to improve our understanding of experience-induced neuroplasticity. NeuroImage 131, 55–72. doi:10.1016/j.neuroimage.2015.08.047.

Tardif, C.L., Schäfer, A., Waehnert, M., Dinse, J., Turner, R., Bazin, P.-L., 2015. Multi-contrast multi-scale surface registration for improved alignment of cortical areas. NeuroImage 111, 107–122. doi:10.1016/j.neuroimage.2015.02.005.

Tisdall, M. D., Hess, A. T., Reuter, M., Meintjes, E. M., Fischl, B., Van Der Kouwe, A. J., 2012. Volumetric navigators for prospective motion correction and selective reacquisition in neuroanatomical MRI. 10.1002/mrm.23228

Todd, N., Josephs, O., Callaghan, M.F., Lutti, A., Weiskopf, N., 2015. Prospective motion correction of 3D echo-planar imaging data for functional MRI using optical tracking. NeuroImage 113, 1–12. doi:10.1016/j.neuroimage.2015.03.013.

Truong, M., 2019. Neuroradiology. doi:10.1007/s00234-019-02242-9.

Turner, R., 2019. Myelin and modeling: bootstrapping cortical microcircuits. Front. Neural Circt. 13. doi:10.3389/fncir.2019.00034.

Vannesjo, S.J., Wilm, B.J., Duerst, Y., Gross, S., Brunner, D.O., Dietrich, B.E., Schmid, T., Barmet, C., Pruessmann, K.P., 2015. Retrospective correction of physiological field fluctuations in high-field brain MRI using concurrent field monitoring. Magn. Reson. Med. 73 (5), 1833–1843. doi:10.1002/mrm.25303.

Versluis, M.J., Peeters, J.M., van Rooden, S., van der Grond, J., van Buchem, M.a., Webb, a.G., van Osch, M.J.P., 2010. Origin and reduction of motion and f0 artifacts in high resolution T2*-weighted magnetic resonance imaging: application in Alzheimer's disease patients.. NeuroImage 51 (3), 1082–1088. doi:10.1016/j.neuroimage.2010.03.048.

Waehnert, M.D., Dinse, J., Schäfer, A., Geyer, S., Bazin, P.-L., Turner, R., Tardif, C.L., 2016. A subject-specific framework for in vivo myeloarchitectonic analysis using high resolution quantitative MRI. NeuroImage 94–107. doi:10.1016/j.neuroimage.2015.10.001.

Wallace, T.E., Afacan, O., Waszak, M., Kober, T., Warfield, S.K., 2019. Head motion measurement and correction using FID navigators. Magn. Reson. Med. 81 (1), 258–274. doi:10.1002/mrm.27381.

Wang, W.T., Hu, P., Meyer, C.H., 2007. Estimating the spatial resolution of in vivo magnetic resonance images using radiofrequency tagging pulses. Magn. Reson. Med. 58 (1), 190–199. doi:10.1002/mrm.21257.

Yeatman, J.D., Wandell, B.A., Mezer, A.A., 2014. Lifespan maturation and degeneration of human brain white matter. Nat. Commun. 5. doi:10.1038/ncomms5932.

Zahneisen, B., Keating, B., Singh, A., Herbst, M., Ernst, T., 2016. Reverse retrospective motion correction. Magn. Reson. Med. 75 (6), 2341–2349. doi:10.1002/mrm.25830.